Entropic stabilization and retrograde solubility in Zn_4Sb_3

Gregory S. Pomrehn, Eric S. Toberer, G. Jeffrey Snyder,* and Axel van de Walle†
Materials Science, California Institute of Technology, 1200 E. California Blvd., Pasadena, California 91125, USA
(Received 21 October 2010; revised manuscript received 12 January 2011; published 4 March 2011)

Zn_4Sb_3 is shown to be entropically stabilized versus decomposition to Zn and ZnSb through the effects of configurational disorder and phonon free energy. Single-phase stability is predicted for a range of compositions and temperatures. Retrograde solubility of Zn is predicted on the two-phase boundary region between Zn_4Sb_3 and Zn. The complex temperature-dependent solubility can be used to explain the variety of nanoparticle formation observed in the system: formation of ZnSb on the Sb-rich side, Zn on the far Zn-rich side, and nano-void formation due to Zn precipitates being reabsorbed at lower temperatures.

DOI: 10.1103/PhysRevB.83.094106 PACS number(s): 81.30.Bx, 64.70.qd, 65.40.gd, 84.60.Rb

I. INTRODUCTION

The Zn-Sb binary phase system has been of interest for many years in the search for efficient and low-cost thermoelectric materials. Of primary interest has been the Zn_4Sb_3 phase which exhibits a thermoelectric figure of merit, zT, in excess of 1 in intermediate temperature ranges.[1] This phase, being composed of environmentally benign and relatively earth-abundant elements, continues to draw active research.

Zn_4Sb_3 exhibits exceptionally low lattice thermal conductivity,[1] due in part to its high configurational disorder. The room temperature structure of Zn_4Sb_3 ($R\bar{3}c$; Fig. 1), denoted β-Zn_4Sb_3 here[1] (or sometimes ϵ-Zn_4Sb_3[2]), contains an anionic framework composed of 30 Sb, divided between 6 Sb_2^{4-} dimers and 18 isolated Sb^{3-}. With 39 Zn^{2+} a charge-balanced composition is obtained at $Zn_{13}Sb_{10}$. Of these Zn cations, at most 36 can fit on Zn framework sites and 3 must be distributed among three crystallographically distinct interstitial sites.[3] For clarity, we will always refer to the entire phase as Zn_4Sb_3 and write Zn_XSb_{10} only when referring to a specific configurational composition within Zn_4Sb_3.

Previous *ab initio* studies of Zn_4Sb_3 have included the electronic density of states and formation energy of various atomic configurations ranging in composition from $Zn_{12}Sb_{10}$ to $Zn_{14}Sb_{10}$.[4–7] These results confirm the expectation from charge counting that $Zn_{13}Sb_{10}$ has a Fermi level in the band gap, Zn-deficient $Zn_{12}Sb_{10}$ has a Fermi level in the valence band, and Zn-rich $Zn_{14}Sb_{10}$ has a Fermi level in the conduction band. All reports of formation energy[5–7] also show agreement that all Zn_4Sb_3 configurations have a positive formation enthalpy at 0 K with respect to Zn and ZnSb. Yet Zn_4Sb_3 is observed below 700 K. Furthermore, at low temperature, a reversible transition to a low symmetry, metastable, ordered α (and α') phase is observed.[8,9]

Synthetically, Zn_4Sb_3 is usually prepared with excess Zn: $Zn_{13.3}Sb_{10}$. As Zn has a high vapor pressure even at the relatively low synthesis and operation temperature, as well as the tendency to readily oxidize,[10] it is not very surprising that excess Zn helps form the phase. Zn_4Sb_3 is always a heavily doped p-type semiconductor with room temperature (Hall) carrier concentration between 6×10^{19} cm^3 and 9×10^{19} cm^3.[11] According to the simple charge counting and *ab initio* calculations, this would be best explained by a slight Zn deficiency, $Zn_{13-\delta}Sb_{10}$, where δ should be between 0.016 and 0.024. If n/n_{Hall} is 2 as predicted by Singh,[4] then δ should be between 0.008 and 0.012. It is perhaps surprising that with all the interstitial Zn sites, synthesis with excess Zn does not produce *n*-type material.

In this work, we expand on previous *ab initio* results to consider a thorough thermodynamic investigation of Zn_4Sb_3. A thermodynamic ensemble approach is necessary because no single configuration (or even small number of configurations) can adequately describe the phase. By assembling a grand canonical partition function we are able to quantitatively prove entropic stabilization. We also predict a region of single-phase stability on a temperature versus composition diagram that exhibits retrograde solubility of Zn with $\delta > 0$ that would always produce *p*-type Zn_4Sb_3 in intermediate temperatures.

II. COMPUTATIONAL METHODS

The natural thermodynamic function to account for a range of possible compositions is the grand canonical potential[12] (GCP):

$$\phi(T,\mu) = -\frac{k_B T}{N} \ln\left[\sum_s e^{-(E_s - \boldsymbol{\mu}\cdot \boldsymbol{N}_s)/k_B T}\right], \qquad (1)$$

where k_B is Boltzmann's constant, T is temperature, N is the total number of atoms in the system, while, for a given state s, E_s is the total energy of state, $\boldsymbol{N}_s$ is a vector containing the number of atoms for each chemical species (with elements summing to N), and $\boldsymbol{\mu}$ is a vector containing the chemical potential of each species. This greatly simplifies for both Zn and ZnSb, which do not exhibit configurational disorder:

$$\phi(T,\mu) = \frac{\varepsilon_0}{n} - \boldsymbol{\mu}\cdot \boldsymbol{x_0}, \qquad (2)$$

where ε_0 is the energy per unit cell, n is the number of atoms per unit cell, and $\boldsymbol{x_0}$ is a vector of the atomic fraction of each species.

For Zn_4Sb_3, we consider the GCP within an independent cells approximation. We assume that each primitive unit cell of 23 ± 2 atoms is noninteracting with neighboring cells, in the sense that the defect configuration present in one cell does not affect the energies of defect configurations in a nearby cell. (All our *ab initio* calculations are nevertheless performed on infinite periodic systems with suitable *k*-point sampling.) This approach is useful in this system because the unit cell is rather large. This assumption is validated by computing the energy of

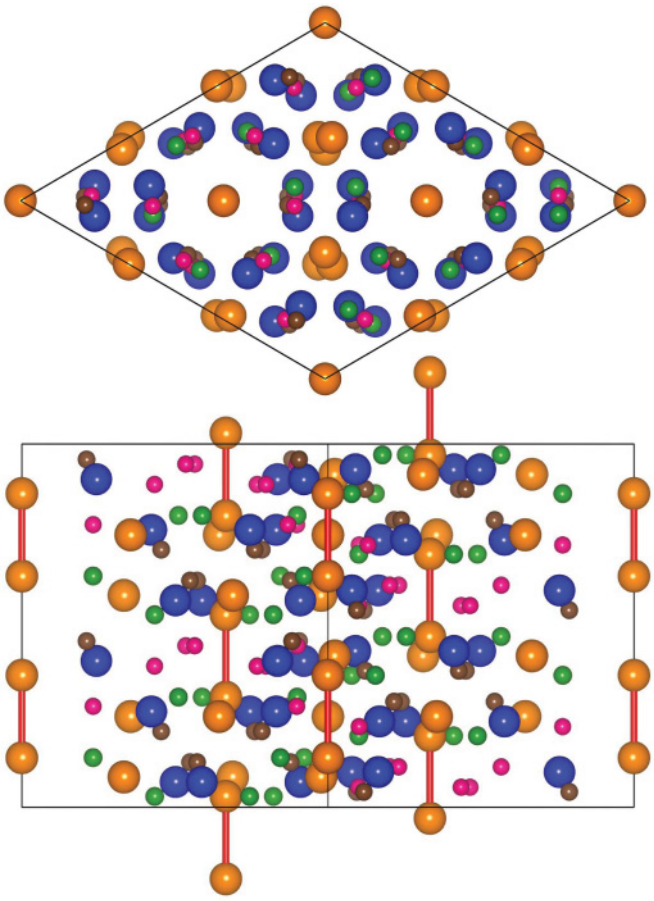

FIG. 1. (Color online) Conventional hexagonal unit cell of Zn_4Sb_3. The Sb sublattice (orange) is composed of isolated Sb and Sb dimers. The Zn "A" sublattice (blue) is 90% occupied. The "B" (green), "C" (brown), and "D" (pink) Zn sublattices are 5% occupied. The primitive rhombohedral cell is 1/3 the volume of the conventional cell.

supercells with different configurations in each primitive unit cell and comparing it to that predicted by summing the energies of the constituent primitive cells. Under the independent cells approximation:

$$\phi(T,\mu)=\frac{\varepsilon_0}{n}-\boldsymbol{\mu}\cdot\boldsymbol{x_0}-\frac{k_BT}{n}\ln\left[1+\sum_{i>0}m_ie^{-(\Delta\varepsilon_i-\mu\cdot\Delta n_i)/k_BT}\right], \tag{3}$$

where ε_0 is the ground-state energy per unit cell, n is the number of atoms per unit cell, and x_0 is the ground-state composition. For each configuration, i, m_i is the symmetric multiplicity, $\Delta\varepsilon_i$ is the change in energy from the ground state, and $\Delta\boldsymbol{n}_i$ is the change in the number of atoms from the ground state.

The energy for each configuration is calculated under the generalized gradient approximation (GGA) using the projector augmented wave (PAW) method with Perdew-Burke-Ernzerhof (PBE) potentials as implemented in VASP 4.6, neglecting spin-orbit coupling. All unit cell parameters and atomic positions were allowed to relax to find the lowest energy configuration to within 10^{-4} eV. A final static calculation was performed for an accurate total energy.

Defect configurations were systematically generated by enumerating defect combinations deviating from the undefected $Zn_{12}Sb_{10}$ structure (A sublattice fully occupied and B, C and D sublattices fully unoccupied). Defect clusters were composed of a combination of vacancies on the A sublattice, and occupation of an interstitial site on the B, C, or D sublattices. Clusters of up to six defects were enumerated, excluding some structures because the defects were too close (nearest-neighbor A and C sites both occupied). After allowing the atomic configuration to relax, the resulting atomic positions were projected onto the closest unrelaxed configuration and any duplicate configurations were excluded in order to avoid overcounting states.

Phonon density of states and vibrational free energies were calculated using the "supercell" method as implemented in the Alloy Theoretic Automated Toolkit (ATAT).[13–15] Since the computational resources needed to compute phonon modes for all Zn_4Sb_3 configurations are prohibitive, representative configurations were selected at four compositions between $Zn_{12}Sb_{10}$ and $Zn_{15}Sb_{10}$ configurations. The lowest-energy configuration for each composition was selected as well as a second $Zn_{13}Sb_{10}$ configuration to assess the error in our approximation. For each of these configurations and the end members Zn and ZnSb, phonon modes were calculated at 0, 1, and 2% strain to account for the effects of thermal expansion, under the quasiharmonic approximation.

The vibrational contribution to the free energy is incorporated into the GCP through a nested sum in the partition function.[16] For each distinct configuration, phonon occupation accounts for small displacements around the local energy minimum, resulting in a temperature-dependent free-energy correction.

GCPs were assembled for Zn, Zn_4Sb_3, and ZnSb. Phase equilibrium is determined by equality of two respective GCPs. The equilibrium composition of each phase can be determined by

$$\nabla_{\boldsymbol{\mu}}\phi(T,\boldsymbol{\mu})=-\boldsymbol{x}. \tag{4}$$

III. RESULTS AND DISCUSSION

Over 100 unique, stable configurations were enumerated in the β-Zn_4Sb_3 primitive rhombohedral unit cell with between 21 and 25 atoms per cell (the number of Sb was held constant at 10). The 0 K formation enthalpy of these configurations with respect to Zn and ZnSb is shown in Fig. 2.

Consistent with previous theoretical studies,[5–7] all configurations have a positive formation enthalpy with respect to Zn and ZnSb. The convex hull is plotted in solid black and connects the ground-state configurations (for Zn_4Sb_3 phase) at each composition. The composition $Zn_{14}Sb_{10}$ does not have a configuration touching the convex hull. This means that for an ensemble of atoms of composition $Zn_{14}Sb_{10}$ constrained to remain in the Zn_4Sb_3 lattice, it would be more energetically favorable to form a mixture of cells of composition $Zn_{13}Sb_{10}$ and $Zn_{15}Sb_{10}$. If the system is allowed to adopt any lattice, then, at 0 K, it would be even more energetically favorable to separate into Zn and ZnSb crystals. Figure 2 also allows us to test the independent cells approximation. The data

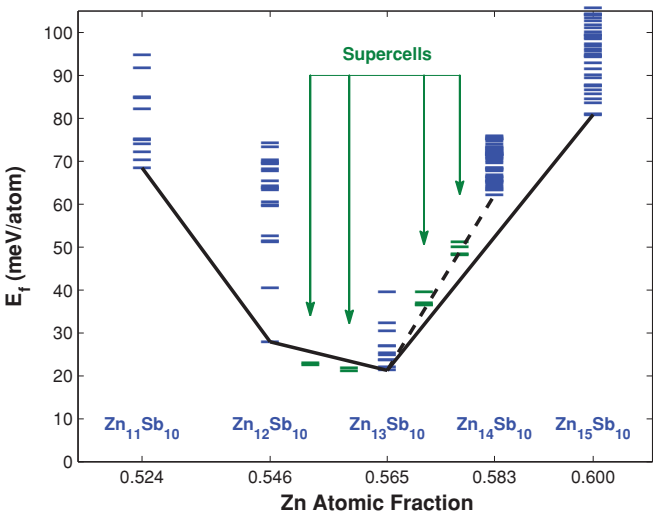

FIG. 2. (Color online) Formation enthalpy at 0 K for Zn_4Sb_3 configurations with respect to Zn and ZnSb. The solid black line represents the convex hull of structures confined to the Zn_4Sb_3 lattice. Supercell calculations in green were done using the conventional unit cell, each composed of three primitive unit cells. The dashed line shows the predicted energy for supercells following the independent cells approximation.

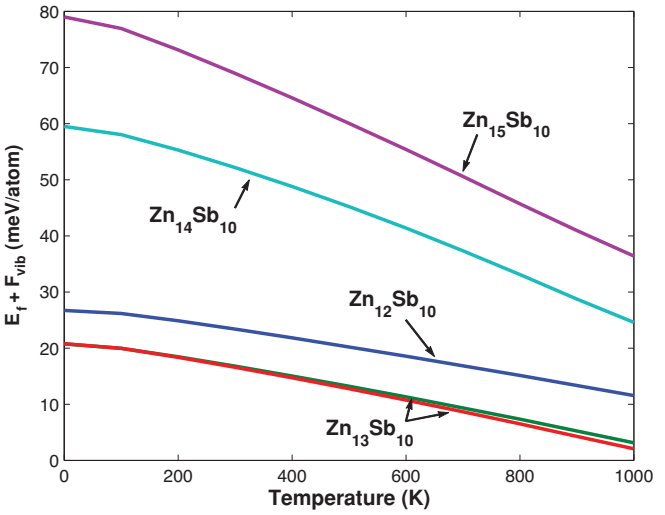

FIG. 3. (Color online) Formation free energy due to phonons with respect to Zn and ZnSb of the lowest energy Zn_4Sb_3 configurations at each composition. There is a more favorable contribution to the formation energy for the more disordered Zn-rich configurations, evidenced by a steeper slope with temperature. Two configurations of $Zn_{13}Sb_{10}$ are in good agreement to 1 meV per atom.

points marked supercells are all made up of three primitive cells of different compositions to yield the intermediate compositions shown. Between $Zn_{12}Sb_{10}$ and $Zn_{13}Sb_{10}$, we see that the supercells produce a slightly lower energy by about 3 meV per atom than predicted by the independent cells approximation. Between $Zn_{13}Sb_{10}$ and $Zn_{14}Sb_{10}$, the energies from the supercells are either very close or slightly higher than predicted by the independent cells approximation (the dashed line). The small energy difference of a few millielectron volts per atom justifies the use of the independent cells approximation, although a consideration of a possible systematic error is discussed later.

The formation free energy due to phonons (relative to Zn and ZnSb) is shown in Fig. 3 for the five representative configurations (the lowest-energy structure at each composition). In all cases, the phonon contribution to the free energy favors the Zn_4Sb_3 phase over Zn and ZnSb as evidenced by a negative trend with temperature. This is likely a result of the softer phonon modes in the more complex and open crystal structure. Increasing Zn concentration and thereby increasing the Zn disorder results in a more favorable contribution to the free energy. There is good agreement between the two configurations of composition $Zn_{13}Sb_{10}$, differing by 1 meV per atom at 1000 K. It then seems reasonable to assume that the vibrational free energy of the representative structures may be applied to all the configurations at that composition when we compute the GCP of Zn_4Sb_3.

The computed region of single phase stability for Zn_4Sb_3 is shown in Fig. 4. Including configurational and vibrational effects to the free energy, Zn_4Sb_3 is found to stabilize at around 700 K at a composition of $Zn_{12.992}Sb_{10}$. As the temperature increases, the range of stable single-phase compositions increases, more broadly on the Zn-deficient side. (Eventually, the solid melts, but our analysis focuses on the solid-state portion of the phase diagram.) Interestingly, on the Zn-rich side, we observe retrograde solubility of Zn. That is, the highest stable concentration of Zn in Zn_4Sb_3 decreases with increasing temperature. This unusual finding is a result of the composition-dependent relationship between the enthalpy and entropy of mixing. Typically defects of all kinds entropically stabilize stoichiometric variations on both sides of a valence precise composition. In the case of Zn_4Sb_3, the valence precise composition is already "defected" with interstitial Zn. A miscibility gap arises for compositions above $Zn_{13}Sb_{10}$

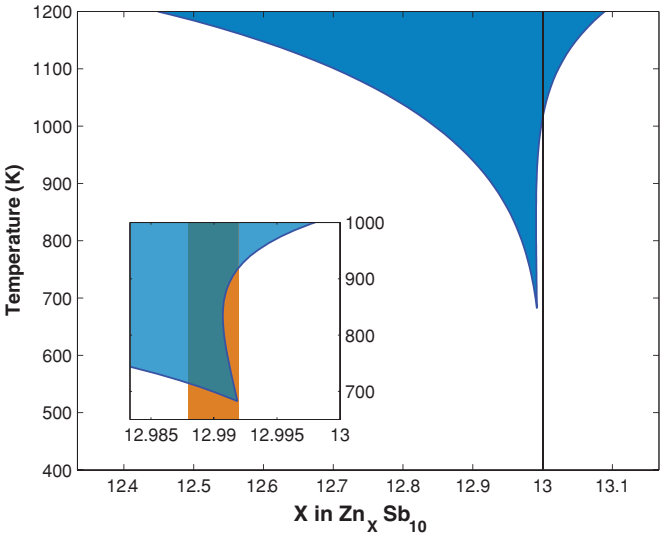

FIG. 4. (Color online) Single-phase stability region for Zn_4Sb_3. Solid black line corresponds to the charge-balanced composition. Stable compositions to the left of the line will result in a *p*-type semiconductor. (Inset) A close-up of the region of retrograde Zn solubility. The orange band corresponds to compositions estimated from charge carrier measurements.[11]

due to the large jump in formation enthalpy compared to the Zn-deficient compositions. The effect is lessened by the counteractive effects of higher vibrational entropy for the Zn-rich compositions. If the vibrational effects were neglected, the Zn-rich boundary would not curve to the right until a much higher temperature.

The region of single-phase stability shown in Fig. 4 has readily observable consequences. The black vertical line at composition $Zn_{13}Sb_{10}$ represents the valence precise structure with a Fermi level inside the band gap. At any Zn-deficient composition from $Zn_{13}Sb_{10}$, we expect a partially filled valence band resulting in a *p*-type semiconductor. (Surprisingly, there is a recent report of a $Zn_{13}Sb_{10}$ configuration being slightly *p*-type.[17] Our electronic density of states results are in agreement with previous studies.[4–7]) All stable compositions below 1000 K in Fig. 4 result in a *p*-type semiconductor. Attempting to dope Zn_4Sb_3 with excess Zn will not result in an *n*-type semiconductor but a two-phase equilibrium between Zn metal and *p*-type Zn_4Sb_3. Furthermore, with the consideration of retrograde solubility, if Zn-saturated single-phase Zn_4Sb_3 is heated up, it passes through a region where it becomes thermodynamically more stable to precipitate Zn metal. With more heating, the Zn is reabsorbed as more Zn-rich compositions are stable. On cooling, the same precipitation and absorption should occur if held in thermodynamic equilibrium.

On the Zn-deficient side of the stable phase region the usual temperature-dependent solubility is observed. Here one would expect ZnSb to precipitate as the temperature is reduced. Because this would occur at low temperatures in the solid state, small nanometer-sized precipitates would be expected. Such particles are indeed observed in Sb-rich samples.[11]

The high-temperature phase boundary on the Zn-rich side could explain the formation of Zn nanoparticles observed in some Zn_4Sb_3 samples.[18] Cooling a Zn-rich composition above $Zn_{13}Sb_{10}$ would precipitate Zn (possibly nanoparticles if cooled fast enough[19]). On further cooling through the retrograde region, some of the Zn would be reabsorbed into the β phase. The absorption of nanoparticle Zn may explain the nano-voids observed in some samples.[11] The precipitation of Zn from the Zn_4Sb_3 structure and then subsequent reabsorption also explains the increase in volume (leading to breakage of the glass ampoule) in some samples that at room temperature appear to be single phase.

Experimental carrier concentration measurements from Toberer[11] from single-phase β-Zn_4Sb_3 samples range from $6 \times 10^{19}/\text{cm}^3$ to $9 \times 10^{19}/\text{cm}^3$. This corresponds to a composition range of 0.002% atomic Zn between $Zn_{12.988}Sb_{10}$ and $Zn_{12.992}Sb_{10}$ assuming $n/n_{\text{Hall}} = 2$[4]. This concentration range, corresponding to the orange band in the inset of Fig. 4, is in close agreement with the predicted stable compositions near the stabilization temperature. This composition range is much smaller than the 0.2% atomic Zn observed by microprobe analysis. This discrepancy is not surprising since the composition range is basically the limit of the microprobe resolution.

There is some expected uncertainty in our predicted temperature of stabilization of Zn_4Sb_3. Our predicted temperature of 700 K is much higher than might be expected. There are several possible explanations for this. One simple possibility is the uncertainty inherent in first-principles calculations using the GGA-PBE functional. There could also be a deficiency in our methodology to fully account for the sources of entropy in such a complex disordered structure. Our enumeration method may underestimate the number of Zn_4Sb_3 configurations by comparing the relaxed structures to the fixed lattice in Fig. 1, which represents, in a sense, a measured average over many possible configurations. The vibrational contribution to the free energy has a significant effect in lowering the stabilization temperature. Assuming a representative structure for each composition might be an underestimate for the more disordered configurations and the effect could be even more pronounced. Last, we noted earlier that the supercells on the Zn-deficient side of $Zn_{13}Sb_{10}$ had slightly lower formation energy than expected under the independent cells approximation. This neglected cell-to-cell interaction (2 meV per atom) could lower the stabilization temperature by several hundred degrees. In either case, we expect the retrograde solubility to remain, and possibly intensify, because the supercells on the Zn-rich side of $Zn_{13}Sb_{10}$ are in good agreement with the independent cells approximation.

To ensure that our finding of a single-phase region for the β-Zn_4Sb_3 lattice is not an artifact of the independent cell approximation, we have conducted separate Monte Carlo simulations based on a cluster expansion Hamiltonian fitted to our database of structural energies. These simulations confirm the presence of a single-phase region over the temperature range where β-Zn_4Sb_3 is stable. Hence, the independent cell approximation was deemed reliable and was used throughout this work. It provides a convenient explicit expression for the free energy and is immune to the fitting errors inherent to the Hamiltonian construction procedure.

Finally, we consider how Zn_4Sb_3 might interact with other nearby phases, namely α-Zn_4Sb_3 and Zn_8Sb_7. A first-principles calculation of α-Zn_4Sb_3 yields positive formation energy of 19 meV per atom with respect to Zn and ZnSb. This is 3 meV per atom below the lowest-energy β-Zn_4Sb_3 configuration of composition $Zn_{13}Sb_{10}$. Assuming no configurational disorder in α-Zn_4Sb_3 we predict β-Zn_4Sb_3 to become energetically favorable compared to α-Zn_4Sb_3 at 300 K (although both are still metastable with respect to Zn and ZnSb at this temperature). It seems possible that there is a temperature range in which metastable β-Zn_4Sb_3 is observed before becoming thermodynamically stable with respect to Zn and ZnSb at some higher temperature.

Another phase of recent interest is Zn_8Sb_7, which has been characterized experimentally and studied through first-principles calculations.[20,21] These calculations reveal that, even though Zn_8Sb_7 is unstable in bulk form, it could be stabilized in nanocrystaline form if surface stress or energy contributions result in a free energy decrease of 5 meV per atom (relative to ZnSb and Zn_4Sb_3). Taking these assumptions into effect, the resulting phase diagram is shown in Fig. 5. We see that Zn_8Sb_7 would stabilize at a temperature higher than Zn_4Sb_3 and a two-phase region results. This also reduces the stable Zn-deficient Zn_4Sb_3 composition range predicted in the absence of Zn_8Sb_7 (dashed line in Fig. 5). Other unidentified phases as reported in some phase diagrams[22] could have a similar effect.

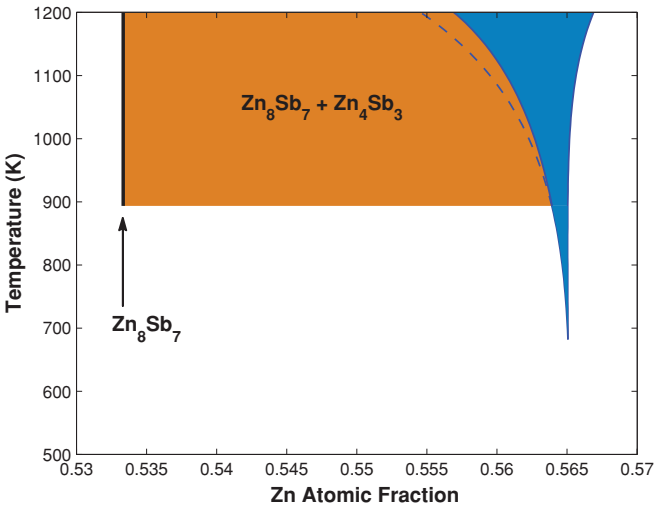

FIG. 5. (Color online) Possible phase-stability regions of Zn_4Sb_3 and Zn_8Sb_7 under conditions favorable to the formation of Zn_8Sb_7. The dotted line represents the phase boundary of Zn_4Sb_3 in the absence of Zn_8Sb_7.

IV. CONCLUSIONS

From our first-principles investigation, we have shown that Zn_4Sb_3 is entropically stabilized with the help of configurational and vibrational entropy. Under the independent cells approximation of the grand canonical potential we predict a region of single-phase stability near $Zn_{12.992}Sb_{10}$, which results in a nominally *p*-type semiconductor. Additionally, we predict a temperature range with retrograde Zn solubility. The temperature-dependent solubility can be used to explain the variety of nanoparticle formation observed in the system: formation of ZnSb on the Sb-rich side, Zn on the far Zn-rich side, and nano-void formation due to Zn precipitates being reabsorbed at lower temperatures.

ACKNOWLEDGMENTS

This work is supported by the US National Science Foundation via Grant No. DMR-0953378, through TeraGrid resources at NCSA and SDSC under Grant No. TG-DMR050013N, and the ARO-MURI Materials on the Brink and the DARPA Nano Materials Program.

*jsnyder@caltech.edu
†avdw@caltech.edu

[1] T. Caillat, J.-P. Fleurial, and A. Borshchevsky, J. Phys. Chem. Solids **58**, 1119 (1997).
[2] G. Nakamoto *et al.*, J. Alloys Compd. **432**, 116 (2007).
[3] G. Snyder, M. Christensen, E. Nishibori, T. Caillat, and B. Iversen, Nat. Mater. **3**, 458 (2004).
[4] S.-G. Kim, I. I. Mazin, and D. J. Singh, Phys. Rev. B **57**, 6199 (1998).
[5] F. Cargnoni *et al.*, Chem. Eur. J. **10**, 3861 (2004).
[6] E. S. Toberer *et al.*, Phys. Stat. Sol. RRL **1**, 253 (2007).
[7] A. S. Mikhaylushkin, J. Nylen, and U. Haussermann, Chem. Eur. J. **11**, 4912 (2005).
[8] J. Nylen, M. Andersson, S. Lidin, and U. Haussermann, J. Am. Chem. Soc. **126**, 16306 (2004).
[9] J. Nylen *et al.*, Chem. Mater. **19**, 834 (2007).
[10] H. Yin *et al.*, J. Electron. Mater. **39**, 1957 (2010).
[11] E. S. Toberer, P. Rauwel, S. Gariel, J. Taftø, and G. Jeffrey Snyder, J. Mater. Chem. **20**, 9877 (2010).
[12] A. van de Walle and M. Asta, Modell. Simul. Mater. Sci. Eng. **10**, 521 (2002).
[13] A. van de Walle, M. Asta, and G. Ceder, CALPHAD J. **26**, 539 (2002).
[14] A. van de Walle, CALPHAD J. **33**, 266 (2009).
[15] A. van de Walle and G. Ceder, J. Phase Equilib. **23**, 348 (2002).
[16] A. van de Walle and G. Ceder, Rev. Mod. Phys. **74**, 11 (2002).
[17] A. N. Qiu, L. T. Zhang, and J. S. Wu, Phys. Rev. B **81**, 035203 (2010).
[18] Ø. Prytz *et al.*, Philos. Mag. Lett. **89**, 362 (2009).
[19] T. Ikeda, V. A. Ravi, and G. J. Snyder, Acta Mater. **57**, 666 (2009).
[20] C. S. Birkel *et al.*, J. Am. Chem. Soc. **132**, 9881 (2010).
[21] G. Pomrehn (unpublished).
[22] V. Izard, M. Record, and J. Tedenac, J. Alloys Compd. **345**, 257 (2002).